Multi-band ESCL transmission supported by bismuth-doped and Raman fiber amplification

Aleksandr Donodin, Elliot London, Bruno Correia, Emanuele Virgillito, Mingming Tan, Pratim Hazarika, Ian Phillips, Paul Harper, Sergei K. Turitsyn, Vittorio Curri, and Wladek Forysiak

Abstract—Ultra-wideband transmission utilizes bandwidths beyond the standard C-band to enable significant network capacity upgrades. Upgrading the standard C-band to a C+L-band transmission scenario is already feasible, and exploratory transmission is being performed in the S-, E-, and O-bands to investigate quality of transmission (QoT) impairments in these spectral regions. In this paper, experimental transmission through a SCL- and partial E-band spectral region is performed, with use of a hybrid amplifier that exploits discrete Raman amplification for the SCL-bands, and a bismuth-doped fiber amplifier (BDFA) for the E-band. Through this transmission bandwidth, we demonstrate that 36 Tbit/s transmission is possible, with 150 coherent channels over 70 km of standard, single-mode fiber. This result is compared to a wideband physical layer model that considers a realistic full spectral load transmission scenario, where the E-band is occupied by 74 channels, providing a total of 221 channels. This comparison demonstrates that, for both scenarios in this experiment, the greatest impairment is present within the S-band, and the addition of the E-band to a SCL-band scenario has a negligible impact upon the QoT within the C- and L-bands.

Index Terms—Bismuth-doped fiber amplifier, BDFA, coherent transmission, multi-band transmission, wideband transmission, Raman amplifier, DRA, Gaussian noise model, wideband model, optical communications

I. INTRODUCTION

THE rate of transmission through optical networks continues to grow incessantly, and this trend is expected to further accelerate in the near future [1]. Consequently, novel technical solutions are continuously required in order to meet this increasing demand. At present, three such solutions are being remarked upon in the literature: spatial-division multiplexing (SDM), the use of higher-order modulation formats, and multi-band transmission (MBT). SDM is typically divided into two approaches: multi-fiber and multi-mode/multi-core fiber, with the first based on the use of more single-mode fibers (SMFs), including dark fibers. This approach becomes

very costly after the dark-fiber infrastructure is exhausted, as it has recently been estimated that approximately $20,000 is required to lay one kilometer of fiber [1], and at least the same amount of money is required for installing one kilometer of the new types of fibers. On the other hand, the multi-mode/multi-core approach requires significant improvements to existing infrastructure, including the deployment of new fiber, and development of novel in-line and transceiver components [2]. Recently, a number of impressive works have reported transmission of higher-order modulation format signals [3], [4], however this may not be a long-term solution as they scale logarithmically with the signal-to-noise ratio (SNR), and are bounded by nonlinear Shannon limit [5].

The third option, MBT, is a practical approach that allows maximization of return-on-investment in existing infrastructures [6], and is a promising candidate for a reliable mid-term solution. The critical challenge for implementing MBT is the development of efficient optical amplifiers beyond the currently used C-band, in order to extend transmission to the L-, S-, E-, O-, and U-bands [7]. Emerging commercial MBT systems typically target transmission either partially or fully within the C+L-bands by expanding current erbium-doped fiber amplifier (EDFA) technology. However, to go beyond this, novel amplifiers in the U-, S-, E-, and O-bands must be developed, together with a large range of components, devices, and sub-systems [8], [9], including novel transmitters and receivers operating in unconventional bands [10], [11].

There have been recent significant advances in the development of new amplifier technologies, such as various doped-fiber amplifiers [12], [13], Raman amplifiers [14], fiber optical parametric amplifiers [15], and semiconductor optical amplifiers [16], providing amplification from the O- to the U-bands. Although amplification of the L- and C-bands can be performed with use of EDFAs, beyond these bands, alternative amplification methods are required. Two types of amplifiers can be highlighted as being exceptionally promising for MBT: the Raman amplifier, and the bismuth-doped fiber amplifier (BDFA).

The Raman amplifier features a flexible operation wavelength, if provided with necessary pump lasers, the ability to create a flat-top or tilted gain shape [14], and has been recently used for ESCL-band transmission over 70 km [17]. In contrast, the BDFA features an extraordinary gain of 38 dB [18], [19], an optical power conversion efficiency higher than 30% [18], and a noise figure as low as 4.5 dB [20]. Moreover, the BDFA provides optical gain in a variety of bands, due to the characteristics of Bi-related centers that depend on the co-

doping materials [21], [22]. Each amplification method has its own advantages and disadvantages, and in the case of Raman amplification, although this enables high power amplification in regions beyond the L- and C-bands, placing the Raman pumps within the spectrum restricts transmission through the spectral regions that the pumps occupy.

Recently, successful coherent transmission in the E-band has been reported solely using BDFAs [23], [24], with the latter work featuring transmission of 143 channels over the ESCL-bands aided by a wide-band Raman amplifier. In these experimental studies, full spectral load transmission is performed in the SCL-bands, but only 4 channels are transmitted in the E-band, a limitation that arises from a lack of optical components in the E-band, especially wavelength selective switches (WSSs).

Beyond challenges in component development, more sophisticated models are needed to evaluate the quality of transmission (QoT) in MBT scenarios [25], [26]. Quantifying QoT is necessary to estimate the possible/achievable capacity increases when expanding the spectrum into new bands, and to evaluate the feasibility of current and future lightpaths (LPs). Consequently, an accurate and reliable model that provides wideband QoT estimation is desirable from a network control perspective.

In this work, we expand upon the experimental study in [24], performing 195 nm transmission of 150x30 Gbaud dual polarisation (DP) 16-QAM signals through 70 km of standard single-mode fiber (SMF), using BDFA amplification in the E-band, and a discrete Raman amplifier (DRA) in the SCL-bands. We then present a wideband model based on a disaggregated derivation of the Gaussian noise (GN) model [27], providing generalized signal-to-noise ratio (GSNR) estimations for an envisaged ESCL-band transmission scenario operating under full spectral load. In this simulation scenario, a total of 221 channels and 26 channels under test (CUTs) are considered for a spectral occupation of 25.8 THz. This model uses an implementation of the open-source GNPy library [28], [29] to model the amplification process and stimulated Raman scattering (SRS) contribution using experimentally-derived parameters, providing the optical signal-to-noise ratio (OSNR) contribution. The nonlinear interference noise (NLI) is estimated using a split-step Fourier method (SSFM) implementation. Combining these two quantities, the GSNR is calculated and used as a figure of merit for the simulated and experimental results.

The remainder of this paper is divided as follows: in Sec. II, an outline of the experimental setup is given, which includes a hybrid amplifier based on a dual-stage SCL-band DRA, and an E-band BDFA. This section also provides details of the data transmission setup. In Sec. III we present the results of experimental transmission of 150x30 GBaud DP-16-QAM through 70 km of SMF. In Sec. IV we describe the main parameters and effects that must be taken into consideration while performing numerical modeling of wideband transmissions. In Sec. IV-C we outline our NLI model, and describe the simulation tools that are used in Sec. V. In Sec. V the SSFM library is introduced, and the key details for the simulation campaign are outlined, such as spectral and optical line configuration parameters. In Sec. VI we present the results of our wideband model for the ESCL system under full and partial spectral load, comparing them to the results of the experimental transmission, and then conclude the paper in Sec. VII.

II. EXPERIMENTAL SETUP

A schematic of the ESCL-band amplifier used within this work is presented in Fig. 1, featuring two separate optical paths for optical amplification: the E-band with a BDFA, and the SCL-bands with a dual-stage DRA. These bands are separated by a filter wavelength division multiplexer (FWDM), which has transmission and reflection bands of 1410-1457 nm and 1470-1620 nm. After band-splitting, the E-band signal follows the upper path in Fig. 1, passing via an isolator to a 300 m long Bi-doped fiber that is bi-directionally pumped by two pump diodes at 1260 nm (forward) and 1310 nm (backward) via a pair of WDM couplers. Two isolators are used to protect the amplifier from back reflection. The Bi-doped fiber used in this paper is the same as reported in [20].

The SCL-band signal follows the lower path in Fig. 1, with the first DRA stage, targeting S-band amplification, consisting of an isolator, a 7.5 km-long inverse dispersion fiber (IDF), a WDM coupler, a pump combiner, and three pump diodes at 1365, 1385, and 1405 nm. The second stage preferentially amplifies the C- and L-bands, and consists of the same set of components, with the exception of the pump combiner, and pump laser diodes at 1425, 1445, 1465, 1485, and 1508 nm [30]. After this, both amplified signals are combined with a 1410-1457 nm/1470-1620 nm FWDM.

The measured gain and NF of the amplifier are presented in Fig. 2, showing a maximum gain of 18 dB in the E-band, and
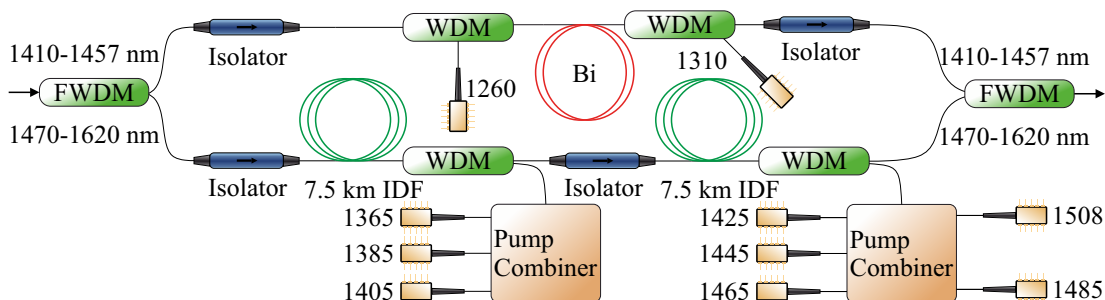

Fig. 1. Experimental setup of the ESCL-band amplifier used within this work, utilizing an active Bi-doped fiber and dual-stage discrete Raman amplification.
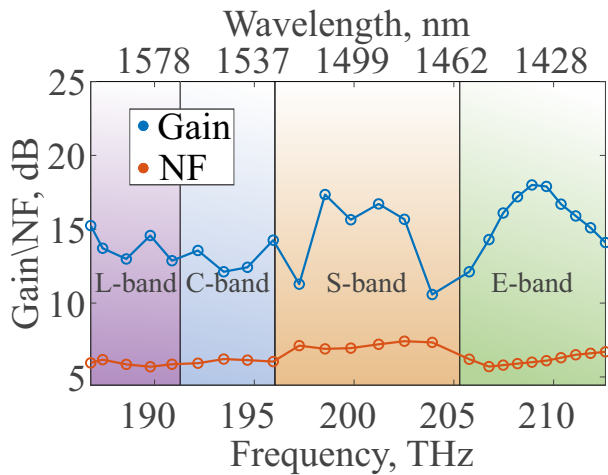
Fig. 2. Gain and NF of the developed ESCL-band amplifier

a minimum NF of 5.9 dB in the L-band. The E-band BDFA was pumped at only 200 mW to provide a matching gain to the DRA. The reduced gain at 1460 nm is explained by the lower efficiency of the BDFA in this region at this relatively low pump power level. The minimum of the NF is at 1450 nm, which corresponds well with the behavior reported previously in [20]. The DRA has increased gain in the S-band, except in the vicinity of 1470 nm and 1520 nm, due to high inter-channel SRS power transfer from S-band to the C- and L-band signals, and pump limitations. The DRA has flat gain (with variations less than 3 dB) from 1520 to 1605 nm, with an average gain of 13 dB in the C- and L-bands.

The setup of the data transmission experiment is presented in Fig. 3: the WDM grid consists of 150x100 GHz channels, including amplified spontaneous emission (ASE) emulated channels in the SCL-bands, and three E-band laser diodes at 1411, 1432, and 1451 nm. The S-band channels (1470-1520 nm) are generated using a supercontinuum source and a commercial wavelength selective switch (WSS) for channel spacing and flattening, followed by a thulium doped fiber am-

plifier (TDFA). The details of in-house made supercontinuum source is provided in the paper by El-Taher et al. [31]. Even though the source operates in S-, C-, L-bands only the S-band part of the spectrum is used to generate dummy channels in this experiment. Two 4 nm and 6 nm guard bands are also present around each of the longest wavelength pumps, located at 1485 nm and 1508 nm, respectively. The S-band channels are combined together with flat channelized C- and L-band ASE noise extending out to 1608 nm, generated using C- and L-band EDFAs and two WSSs for equalization and flattening. Following this, a dense WDM grid is combined with three coarse WDM (CWDM) E-band channels at 1411, 1432, and 1451 nm and the data carrier. The CWDM limitation in the E-band arises predominantly due to the present unavailability of commercial an E-band WSS.

The transmitter and receiver used for this multi-band experiment were originally designed for C+L-band operation, and as such show performance degradation in the S- and E-bands [32]. The data carrier signal is generated using different tuneable lasers operating from 1410 to 1605 nm, which are modulated by a C+L Lithium-Niobate DP IQ modulator, driven by a digital-to-analog converter (DAC), producing a 30 GBaud DP-16-QAM signal with with roll-off factor of 0.1. The signal after the modulator is amplified by a booster amplifier (in-house BDFA for the E-band, commercial TDFA for the S-band, and commercial EDFAs for the C- and L-bands). For power equalization of the data channel with the WDM grid, a variable optical attenuator (VOA) is used ahead of a 90/10 coupler. As the WDM grid is dense in the SCL-bands, the WDM channel corresponding to the data carrier signal is turned off using the WSS to avoid channel overlap. For back-to-back (B2B) transmission, the signal is then directed to an optical bandpass filter (OBPF), where the data carrier is filtered. When transmission is performed, the signal passes into a 70 km span of SMF, followed by the hybrid amplifier. In both cases, after filtering by the OBPF, the data carrier is amplified by an appropriate receiver amplifier, similarly to the booster. The input power into the coherent
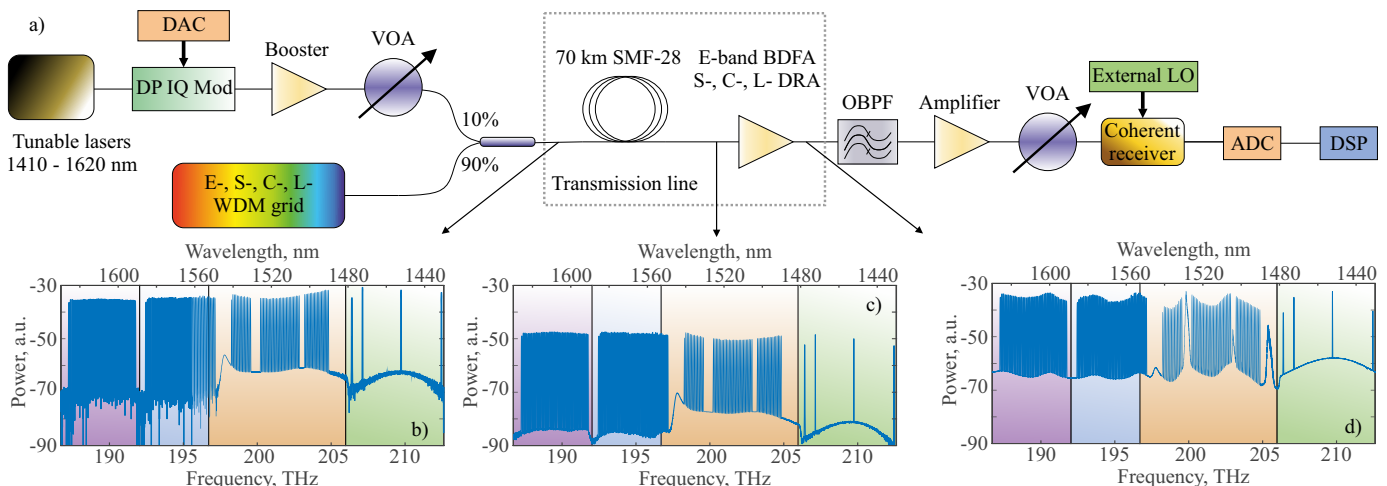

Fig. 3. a) Experimental setup of a B2B and transmission experiment; spectra of the WDM grid and E-band data carrier signal at 1457 nm at (b) input to the span, (c) end of the span, and (d) after the amplifier.

receiver is controlled by another VOA, and a set of external tuneable lasers operating from 1410-1605 nm is used as a local oscillator for the coherent detection transceiver. Receiving the channels is completed by a standard C+L-band hybrid, a set of C+L balanced detectors, and a set of 80 GSa/s analog-to-digital converters (ADCs). The digital signal processing (DSP) chain used for analysis of the received signal has been described previously in [33].

III. EXPERIMENTAL RESULTS

The findings from our experimental transmission are presented in in Fig. 4. First, the wavelength dependencies of the Q^2-factor(averaged over the X and Y polarisations) for 30 GBaud DP-16-QAM are investigated for both the B2B and 70 km long transmission. The measurement is performed in a broad spectral range of 25.83 THz (equivalent to 195 nm) spanning from 1410 to 1605 nm using wavelength-tuneable lasers for both the signal and local oscillator sources. The Q^2-factor is calculated from the bit-error rate of the communication channel transmitting different symbols [34].

The best B2B performance is achieved in the C-band, enabled in this experiment by commercial EDFAs, while L-band B2B performance is decreasing at lower frequencies. The B2B performance in the S-band shows similar performance to the L-band, however, a noticeable decrease of the S-band B2B performance is observed at around 204 THz (1470 nm), which is due to the relatively high NF of the TDFA in this region.

The B2B performance in the E-band has been measured by two in-house BDFAs that are reported in [23]. In general, it is similar to the L-band case, but with a significant performance decrease at 1410 nm, which can be explained by substantial polarization balance limitations that arise from the optical hybrid and IQ modulator, starting at 1420 nm. The X and Y polarization imbalance penalty is presented in Fig. 4 (b), showing a significant increase of the X and Y impairment below 1430 nm. Note that the gain of BDFAs has been shown to be almost polarization independent ($< 0.6dB$) [35]. The commercial optical hybrid and the IQ modulator used in this experiment was optimized for operation in the C- and L- optical bands. There are two main reasons which lead to the poorer performance of optical hybrids beyond the intended range: wavelength limitations of polarization beam splitters, and wavelength dependence of the phase difference introduced by the optical hybrid, which should be 90° in a perfect scenario. For the IQ modulator, only the first reason is applicable as the 90° variation is tuneable. Despite the limited operation bandwidth, the X–Y impairment is lower than 0.6 dB in the whole region from 1430 to 1605 nm.

The transmission performance in the L-band features a Q^2-factor penalty no higher than 2.2 dB, and the lowest Q^2-factor penalty for the whole DRA is only 1 dB, visible in Fig. 4 (b). In the C-band the DRA has a maximum Q^2-factor penalty of 1.7 dB. The DRA in the S-band has a maximum penalty of 3.3 dB and a minimum of 2 dB. The increase of the Q^2-factor penalty at 1470 nm is due to the high NF and nonlinear interference in the DRA in this band of operation which is explained in detail in Sec. VI. The E-band transmission features the lowest Q^2-factor penalty of just 0.5 dB. Otherwise, the general performance of the in-line BDFA is similar to the C- and L- band DRAs. The increasing penalty towards 1410 nm is explained by a correspondingly increasing NF, decreasing amplifier gain, and, most importantly, the polarization imbalance of signal, which occurs due to the polarization sensitivity of the transmitter and receiver components. Through this setup, transmission is performed for a total of 36 Tbit/s (2 x 4 bits x 30GBaud x 150 channels). It should be noted that the E-band performance limitation mostly arise from the B2B performance, and can be fixed with suitable E-band receiver and transceiver components which are currently commercially unavailable.
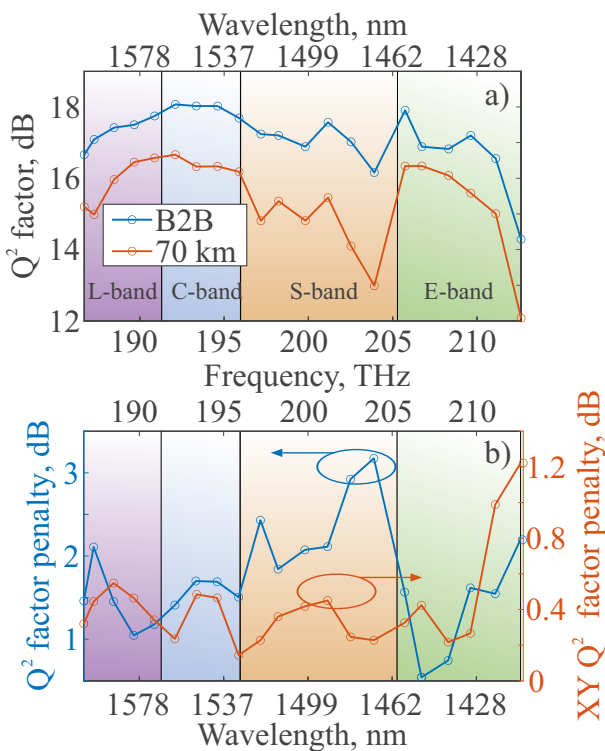
IV. WIDEBAND PHYSICAL LAYER MODEL

To produce an accurate and reliable model of wideband transmission it is important to first precisely describe the significantly contributing optical phenomena that occur during signal transmission through the fiber, which corresponds to correctly defining the physical layer parameters. Considering the amplification process, the BDFA can be represented as a lumped amplifier with an active fiber of negligible length. On the other hand, the physical processes in the Raman amplifier must be considered carefully, as it is a dual stage amplification process through a total of 15 km of fiber, which introduces additional nonlinear impairments [36], [37]. The fiber parameters for both the SMF and IDF are obtained from

Fig. 4. a) Wavelength dependence of the Q^2-factor for the B2B case and 70-km long transmission; b) wavelength dependence of Q^2-factor penalty between B2B case and transmission (blue line with circles) and X and Y polarization Q^2-factor imbalance (orange line with stars)
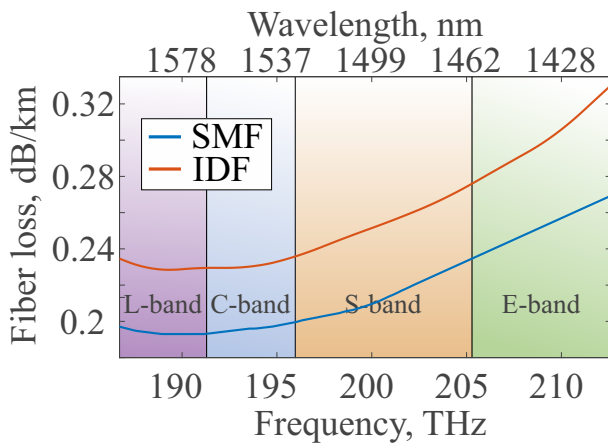
Fig. 5. The loss coefficients, α, of the fibers used within this work as a function of frequency in the ESCL-bands.

experimental data [38], and theoretical models that have been enhanced with data provided by the fiber suppliers.

A. SMF and IDF Parameter Model

To produce an accurate and reliable replication of the experimental transmission described in Sec. II, it is necessary to properly consider the frequency dependency of the fiber parameters, for both the SMF and IDF types, for the wideband spectrum under consideration. The most relevant parameters from a modeling perspective are: the fiber loss coefficient, α, the propagation constant, β, the nonlinear coefficient, γ, and the reference Raman gain coefficient, g_0. More details about the origin and/or derivation of these parameters are given in [25].

Starting with α, this parameter takes into account the power attenuation of the optical signal when propagating through the optical fiber. In this work, we use α values that have been retrieved from experimental measurements performed with a cut-back technique. The full profile over the ESCL-band spectral region is presented in Fig. 5 as the blue line for SMF and the red line for IDF.

Considering next β, this parameter encompasses the dependence of the fiber refractive index upon the frequency of the propagating radiation, which produces dispersive effects. These effects can be represented by a Taylor series expansion, with terms which correspond to the group velocity dispersion, β_2, which is the second derivative of β with respect to the frequency, and describes the broadening behavior of the pulse. In this work, values of β_2 are measured for the SMF and IDF over the required ESCL-band spectral range, and are presented in Fig. 6.

The nonlinearity coefficient, γ, weights the contributions that arise from nonlinear propagation of the signal through the fiber, and may be calculated using:

$$\gamma(\lambda) = \frac{2\pi}{\lambda} \frac{n_2}{A_{\text{eff}}(\lambda)} , \qquad (1)$$

where n_2 is the nonlinear refractive index, and A_{eff} is the fiber effective mode area. As the SMF is a weakly guiding fiber, A_{eff} can be calculated from the theory of weakly guiding fibers [39] using standard SMF parameters: a core radius of 4.2 µm, numerical aperture (NA) of 0.14, and the cladding refractive index determined with the Sellmeier equation with coefficients that correspond to pure silica glass [40]. Combined with a n_2 value of $2.6 \cdot 10^{-20} m^2/W$, γ is calculated for the considered wideband spectrum, and presented in Fig. 7. This parameter is observed to scale almost linearly with frequency, increasing from 1.15 1/W/km in the L-band to 1.45 1/W/km in the E-band for the SMF type.

Lastly, g_0 provides the Raman gain at a reference frequency, f_{ref}, determining the efficiency of the SRS effect, which produces power transfer between channels during transmission, and from the pumps to the amplified channels within the Raman amplification process [41]. This variable has been measured experimentally, for both fiber types, and is presented in Fig. 8. We remark that, for all bands, a maximum value is found at ~ 13 THz, which corresponds to the peak of the efficiency of the SRS effect.
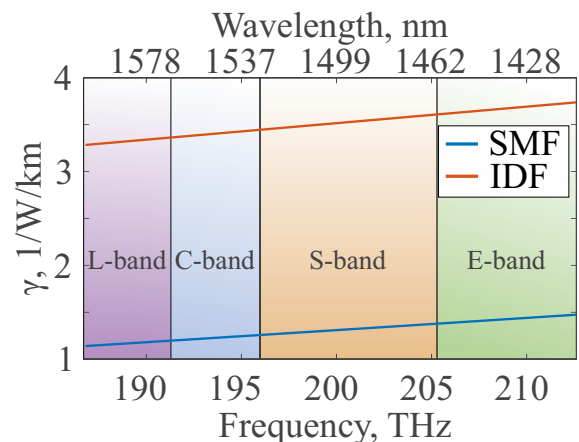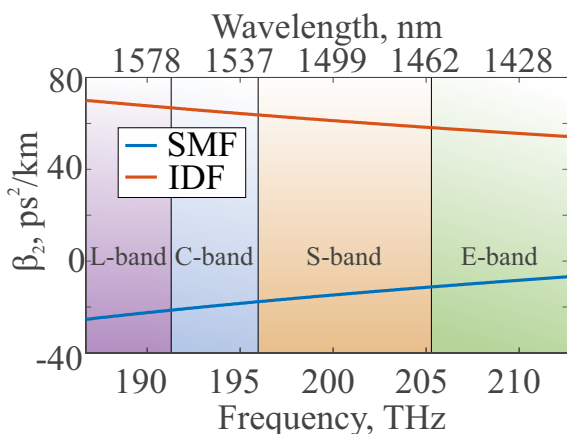

Fig. 6. The group velocity dispersion, β_2, of SMF and IDF as a function of frequency in the ESCL-bands.

Fig. 7. The nonlinear coefficient, γ of SMF and IDF as a function of frequency in the ESCL-bands.
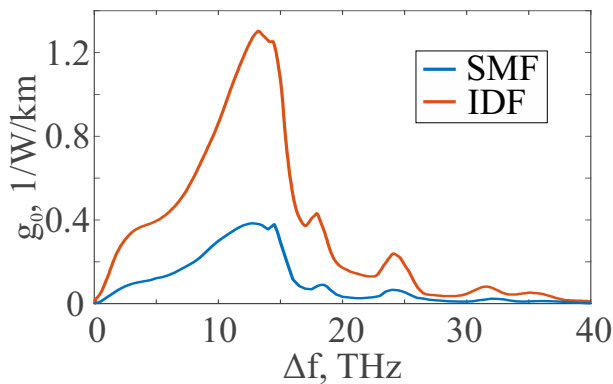
Fig. 8. The reference Raman gain coefficient, g_0, corresponding to the Raman gain at a reference frequency, $f_{\text{ref}} = 203.9\,\text{THz}$, for the two fibers used within this work, as a function of frequency.

B. Amplifier Model

The experimental hybrid amplifier provides gain in the SCL-bands with dual-stage Raman amplification and a BDFA in the E-band. To model the Raman amplifier, transmission through two 7.5 km-long IDF segments is considered, with the counter-propagating pumps assigned wavelength and power values that are specified in Tab. I. In total, eight Raman pumps are used; three within the first IDF for the S-band amplification, and five within the second IDF for the C- and L-bands. The effects of these Raman pumps are included within the amplifier model by solving the Raman equations, which is performed using the RamanSolver module of the GNPy library [29]. This solution provides the power profile for both IDF stages, along with the ASE noise contributions, giving the total OSNR contribution.

For the E-band amplification using the BDFA, due to the short length of fiber involved, a more simple approach resembling that of a standard lumped amplifier (C-band EDFA) is used, where the signal is amplified using the experimentally derived gain and NF profiles. The gain and NF values for each CUT, as calculated using the amplifier model, are presented in Fig. 9. Good approximations of the experimentally measured gain/NF values presented in Fig. 2 are observed, with some notable differences being a much higher E-band gain due to propagation of a full spectral load (the different pumping conditions of the BDFA from the experiment are used in the modeling to fully recover loss of the transmitted E-band signals), and a higher gain and NF within the S-band as a consequence of inter-band effects producing additional loss, which is explained in greater detail in Sec. VI. Achieving very

TABLE I
WAVELENGTHS AND PUMP POWERS FOR EACH RAMAN AMPLIFIER STAGE

Stage	Wavelength	Pump power
S-band	1365 nm	485 mW
S-band	1385 nm	333 mW
S-band	1405 nm	116 mW
C+L-band	1425 nm	205 mW
C+L-band	1445 nm	215 mW
C+L-band	1465 nm	190 mW
C+L-band	1485 nm	47 mW
C+L-band	1508 nm	122 mW

close matching of the both Gain and NF of such a system is a complex task due to various factors that impact these parameters. The aim in this work was to achieve matching of the general trends of the parameters, i.e. high S-band NF, or replicate the ripples in the gain spectrum. To find the BDFA gain/NF profile, several characterization curves with various pump powers are considered and evaluated in terms of average gain. The profile which provides an average gain that most closely compensates for the propagation loss is then selected to be used in the simulation campaign.

C. Physical Layer

To estimate the experimental QoT impairments, a semi-analytical physical layer model that separately provides the linear and nonlinear contributors is presented, based on the methodology described in [25]. The QoT for a given CUT wavelength, λ, through a single fiber span is commonly quantified using the generalized signal-to-noise ratio (GSNR):

$$\text{GSNR} = \left(\text{OSNR}^{-1} + \text{SNR}_{\text{NL}}^{-1} \right)^{-1}, \qquad (2)$$

where the OSNR is the optical signal-to-noise ratio, which encompasses all linear contributions to the overall GSNR, primarily the ASE noise, and SNR_{NL} is the nonlinear signal-to-noise ratio, which includes all nonlinear effects which occur during propagation and corresponds exactly to the NLI impairment.

The generation of NLI is more complicated in MBT scenarios as it depends upon the powers of the CUTs and interfering channels, which are significantly affected by SRS power transferring effects and frequency-dependent α, β, and γ parameters, as defined in Sec. IV. Additionally, calculation of the ASE noise requires an amplifier model that properly takes into account the gains and NFs of the amplifiers within each band, which further induces a frequency dependence upon the power profile.

A first step towards an accurate model of this complex interaction is to tackle the power transfer arising from the SRS effect. By approximating the SRS efficiency function,
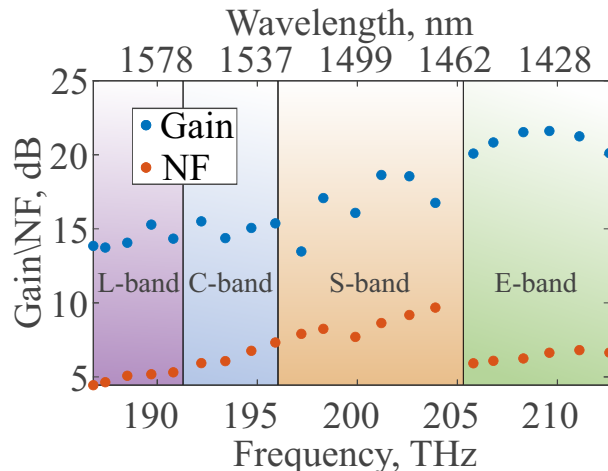

Fig. 9. The gain and NF profiles for the entire spectrum considered within the amplifier model.

accurate closed-form solutions have been presented and verified in [42]–[44], however, this approximation becomes invalid when the CUT and interfering channel are separated by more than 13 THz, which corresponds to the peak of the SRS spectral efficiency. An alternative approach which is used in this work is to start with the generalized Gaussian noise (GGN) model and solve the Raman equations directly, in order to obtain the SRS efficiency function semi-analytically, as performed in [25].

Considering an optical line system that consists of a single fiber span, followed by a hybrid Raman and BDF amplifier, the OSNR and SNR_{NL} contributors to the GSNR, for a given wavelength, λ, are:

$$\text{OSNR} = \frac{P_n}{P_{\text{ASE}}} \, , \tag{3}$$

$$\text{SNR}_{\text{NL}} \leq \frac{P_n}{P_{\text{NLI}}} \, , \tag{4}$$

where P_n is the total channel power, P_{ASE} is the total ASE noise power, and P_{NLI} is the total NLI noise power. Eq. 4 is presented with an inequality symbol due to the coherency of the NLI contributor, meaning that this quantity represents an upper bound.

Concerning the OSNR, as the ASE noise is the significant linear noise contributor, in this scenario the OSNR is given simply by the ratio of the total channel power to the ASE noise contribution. For a constant spectral load, the ASE noise for transmission through a single span of fiber is given by:

$$\text{P}_{\text{ASE}} = h f_c \zeta (G - 1) R_s \, , \tag{5}$$

where h is Planck's constant, and for a channel at a given wavelength λ: f_c is the central frequency of the channel, ζ and G are the amplifier noise factor (linear NF) and linear gain at f_c, and R_s is the channel symbol rate. Eq. 5 may be used to calculate the ASE noise contribution of the BDFA in the E-band, but for the SCL-bands it is calculated from [41], using the evolution of the power profile, which is in turn calculated by solving the Raman equations. We note that all parameters required for Eq. 5 and the Raman equations are obtained from experimental characterization of the amplifier. Specifically, f_c is obtained by analysis of the spectrum, ζ and G are measured for all wavelengths under investigation, for a variety of input powers, and R_s is a constant 30 GBaud for all channels.

The total NLI noise power, P_{NLI}, is the sum of the noise induced by the single-channel (SC), P_{SC}, and cross-channel (XC), P_{XC}, contributors [45]:

$$\text{SNR}_{\text{NL}} \geq \frac{P_n}{P_{\text{SC}} + P_{\text{XC}}} \, , \tag{6}$$

which can be given in terms of the NLI efficiency, η, for a given wavelength under test, λ, and an interfering wavelength, κ:

$$P_{\text{SC}} = \eta_\lambda P_\lambda^3 \, , \tag{7}$$

$$P_{\text{XC}} = \eta_{\lambda\kappa} P_\lambda P_\kappa^2 \, , \tag{8}$$

where P_λ is the total channel power over all polarization states for a wavelength λ. The quantities η_λ and $\eta_{\lambda\kappa}$ emerge from the derivation of the PMD-Manakov equation [46], [47]. We

direct readers seeking further detail about the derivation of these parameters to [25], as a full derivation is outside the scope of this work. As transmission is performed over a single span of fiber, typical issues which arise due to the coherent accumulation of the SC contributor are not present [45], meaning that the total NLI power of the WDM signal can be found by separately calculating the SC and XC impairments, for each CUT, producing a superposition of effects [48].

V. SIMULATION DETAILS

Regarding the OSNR contribution to the GSNR, this is calculated with help of the GNPy RamanSolver module, which calculates the ASE noise for each channel using Eq. 5, whereas a SSFM simulation campaign is performed to estimate the SNR_{NL} contribution. This simulation tool, which is based on [46], solves the dual-polarization Manakov equation, and is chosen as the method of NLI estimation in order to preserve maximum accuracy. The dual-polarization Manakov equation is given by [47], [49]:

$$\partial_z \vec{A}(z,t) = \left(-\hat{\alpha}(z) + \iota\hat{\beta} \right) \vec{A}(z,t) \\ -\iota \frac{8}{9} \hat{\gamma} \left[\vec{A}(z,t) \cdot \vec{A}^*(z,t) \right] \vec{A}(z,t) \, , \tag{9}$$

where $\vec{A}(z,t)$ is the dual polarization modal amplitude at position z for a given time t, $\hat{\alpha}(z)$, $\hat{\beta}$, and $\hat{\gamma}$ are the gain, dispersion and nonlinearity coefficient operators, respectively. A numerical solution is found by taking an average of the random birefringence and polarization mode dispersion, and calculating the changes to the WDM signal by iterating through successive, variably-sized dz steps along the fiber.

A. Simulation Parameters

For the experimental transmission, the SCL-bands were fully populated with channels, whereas only four channels were present in the E-band, causing this latter band to produce a comparatively small impairment. To provide a meaningful characterization of the E-band, a fully loaded E-band spectra was considered for the wideband model, producing a spectrum with 41, 46, 60, and 74 channels in the L-, C-, S-, E-bands, respectively, giving a total of 221 channels ranging from 186.8 to 212.6 THz, and a total bandwidth of 25.8 THz, including guard bands at the same positions as those used within the experimental setup. This model therefore aims to provide an estimate of anticipated losses over the entire ESCL-band spectrum for an envisaged full spectral load implementation.

In the experimental setup, a flat power of approximately -2 dBm per channel is used for all bands. This power profile does not represent an optimized transmission scenario due to the complex interplay between the frequency-dependent fiber and amplifier parameters, the NLI, and the SRS power transfer. Finding the optimal input power for each channel within a wideband spectrum has previously been investigated, with promising results seen with the use of evolutionary algorithms [50], [51].

For our model, we choose a middle ground between these two approaches, by calculating the local-optimum global-optimum (LOGO) power [52] for each band. Using this

technique, the average amplifier NF per band is calculated and used to find the optimal working point of the system. This provides an optimally flat power for each band, representing an improvement over a flat value over the entire spectrum, but with comparable results to the experiment performed in Sec. III. The LOGO powers for each band are found to be -1.2, -1.6, -1.3, and -1.0 dBm per channel, for the L-, C-, S-, and E-bands, respectively. The highest power is found for the E-band, demonstrating that a greater input power is required due to the larger group velocity dispersion within this region, as seen in Figs. 5 and 6.

Concerning the line description, we closely replicate the one described in Sec. II, with two distinct transmission stages: a 70 km fiber span covering the ESCL-bands, followed by two 7.5 km fiber spans covering the SCL-bands, representing the propagation and amplification stages, respectively. The description of these fibers is given in a JSON [53] format, providing the required frequency dependent variables, including loss, dispersion, and power profile evolution, which is calculated using the GNPy RamanSolver module.

For the CUTs, in this simulation they are placed within the 100 GHz WDM grid, in locations that correspond as close as possible to the experimental CUTs. Simulating the entire L-, C-, S-, E-band spectrum at once has a prohibitively high computational cost due to large spectral and spatial resolution requirements. However, the amount of NLI generated by an interfering channel upon a CUT falls off sharply with respect to the spectral separation between these two channels, with the majority of the contribution lying withing a 1 THz bandwidth centered around the CUT [54]. To reduce computational costs without a significant loss in accuracy, and to be maximally conservative, a 3 THz window is considered for each CUT centered at each f_c, meaning that NLI contributions from channels lying outside of this bandwidth are not included. Each channel is transmitted with a 16-QAM modulation format, with a roll-off of 0.05, symbol rates of 30 GBaud, and channel bandwidths of 100 GHz.

B. Receiver and DSP

A DSP-based receiver is placed at the termination of the simulated optical line in order to calculate the nonlinear impairment. This receiver first uses an idealized ADC, and each CUT is filtered using two samples per symbol. Dispersion compensation is then applied for each fiber span, recovering all accumulated dispersion upon the CUT. Next, the signal passes to an adaptive equalizer that converges to a matched filter. This equalizer makes use of a least-mean squares (LMS) algorithm with 42 taps and an adaption coefficient of 10^{-4} [55]. This large number of taps is chosen so that there is a high sensitivity to the amount of NLI generated, maximizing its recovery.

Following this, the signal is processed by a carrier phase estimation (CPE) module, which recovers the nonlinear phase noise by comparing the transmitted and received signals. The carrier phase is recovered through an algorithm which dynamically sets the CPE tap length using knowledge of the transmitted symbols, maximizing the circularity of the noise clouds within the transmitted symbol scattering diagram. This

optimal CPE tap length therefore maximizes the accuracy of the recovered NLI noise contribution that arises from the fiber propagation. Lastly, the error vector magnitude (EVM) is calculated upon the signal constellation using one sample per symbol. As the OSNR is calculated outside of the SSFM, this EVM corresponds exactly to the SNR_{NL}, which may then be combined with the OSNR to give an estimation of the GSNR.

VI. MODEL RESULTS

The power profile calculated using the GNPy RamanSolver module at the inputs/outputs the SMF and IDF is given in Fig. 10. Starting with the input power spectrum, given by the blue dots, slightly different levels are visible for each band due to different LOGO input powers. The signal begins transmission by passing through the SMF, producing a power profile given by the orange dots. Here, the impact of the fiber parameters is visible: as the frequency increases, a corresponding reduction in power is observed, evident from the attenuation profile given in Fig. 5.

Low frequency part of the signal then propagates through the first IDF, giving a power profile in yellow. During this transmission, the S-band is amplified, with small amounts of residual amplification also present within the L- and C-bands. When the spectrum propagates through the second IDF, the Raman pumps located within the S-band amplify the L- and C-bands, producing the final power profile, given by the purple dots, which also includes the E-band power profile from the BDFA amplification. Besides some small ripples in the SCL-bands due to the Raman amplification process, which are also visible in the final spectrum in Fig. 3, the overall gain is relatively uniform and flat, demonstrating that the input power has been recovered well.

A. Linear and Nonlinear SNR

The OSNR, SNR_{NL}, and simulated GSNR, $GSNR_{SIM}$ values for the entire fully loaded spectrum are shown in Fig. 11. Firstly, regarding the OSNR, this value is calculated from the ASE noise that is generated during the propagation and
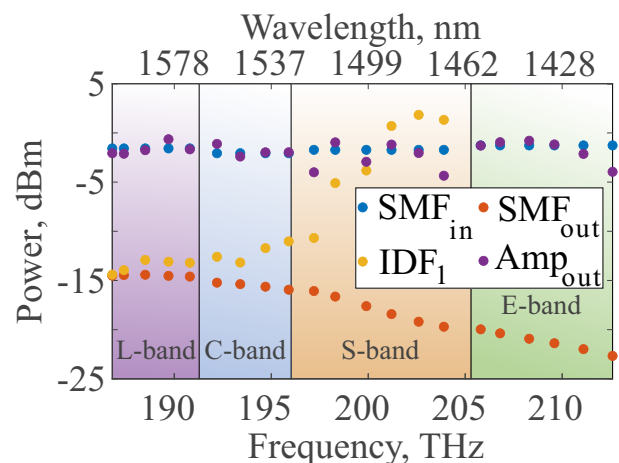

Fig. 10. The power profile of the signal at various points of transmission.

amplification stages. To model the propagation stage, the initial contribution is found by estimating the noise floor for each channel using the input spectrum provided in Fig. 3(b), and re-scaling these values to suit the LOGO powers that were used for the optimized simulated transmission.

In the amplification stages, the GNPy RamanSolver module is used to calculate the total amount of ASE noise, for both the Raman pump and BDFA amplification methods. It is visible that the OSNR is highest in the L- and C-bands, which is entirely a result of the channels within these bands having lower noise floors, therefore generating less ASE noise during propagation. The opposite reason explains the S-band having the worst noise floor, whereas the OSNR in the E-band is dominated by the ASE noise that is generated during the BDFA amplification process.

Regarding the SNR_{NL}, these values are calculated in the SCL-bands by summing the separate contributions from the SMF and IDF, whereas the E-band value corresponds to the NLI generated during SMF transmission, as NLI contributions during BDFA amplification are negligible. The E-band is observed to exhibit significantly better SNR_{NL} performance than all other bands due to this reason.

On the other hand, the worst and most uneven performance is observed within the S-band, which can be explained by analyzing the power profile evolution in Fig. 10. Considering that the XC contributor is dominant for any given CUT, the leading term of the NLI contribution therefore scales with respect to $P_{CUT}P_{ch}^2$, for all interfering channels (see Eq. 8). This means that a greater amount of power at a given channel generates a greater amount of NLI for all neighboring channels. The NLI generated within the S-band is therefore large, primarily due to the Raman pump amplification being performed first in this band, which causes the S-band to enter the second IDF with a relatively large amount of power. This is also evident by considering that the best performance within the S-band corresponds to the region with the lowest gain after transmission through the first IDF.

Better performance in the L- and C- bands is seen for precisely the opposite reason: as the Raman pump amplification

of these bands is performed predominantly in the second IDF, the majority of their propagation is performed at relatively low powers, meaning that the NLI generation is lower. It is also evident that the C-band suffers from the ripples of the S-band amplification performed within the first IDF, whereas the L-band is less affected, resulting in it having the overall best performance.

Regarding the $GSNR_{SIM}$ values, for the L- band the OSNR and SNR_{NL} values have similar contributions, whereas in the C-band the SNR_{NL} dominates, indicating heightened NLI generation during transmission. For the S-band, the asymmetric generation of NLI throughout the band makes the ASE noise and NLI noise the dominant contributors in the lower and upper halves of the (frequency) band, respectively. As for the E-band, $GSNR_{SIM}$ practically overlaps the OSNR value, as the SNR_{NL} that is generated during the SMF transmission and BDFA amplification is negligible.

B. Experimental Validation

As described in Eq. 2, the GSNR is calculated from the OSNR and SNR_{NL} contributions, but to properly compare this simulated value to the experiment, it is necessary to include the B2B transceiver impairments present within the experimental setup. As a final figure of merit a total GSNR which includes these impairments, denoted $GSNR_{TOT}$, is calculated, given by:

$$GSNR_{TOT} = \left(GSNR_{SIM}^{-1} + GSNR_{SYS}^{-1}\right)^{-1}, \quad (10)$$

where $GSNR_{SYS}$ is the system GSNR, which gives the B2B impairment for each CUT. The B2B impairment is characterized experimentally, providing a $GSNR_{SYS}$ value for every CUT (presented in Figure 4,a).

A comparison between $GSNR_{TOT}$ and the experimentally achieved SNR_{exp} is given in Fig. 12. As a first observation, it can be seen that for all bands except the S-band, $GSNR_{SYS}$ is the leading contributor to $GSNR_{TOT}$, which is evident by
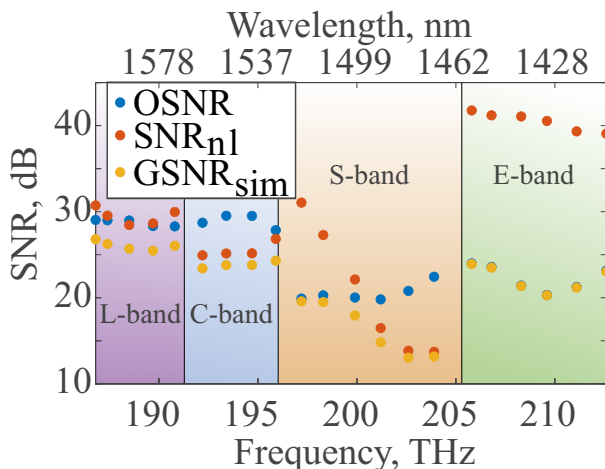

Fig. 11. The OSNR, SNR_{NL}, and $GSNR_{SIM}$ values after propagation and amplification using the combined SCL-band Raman and the E-band BDFA.
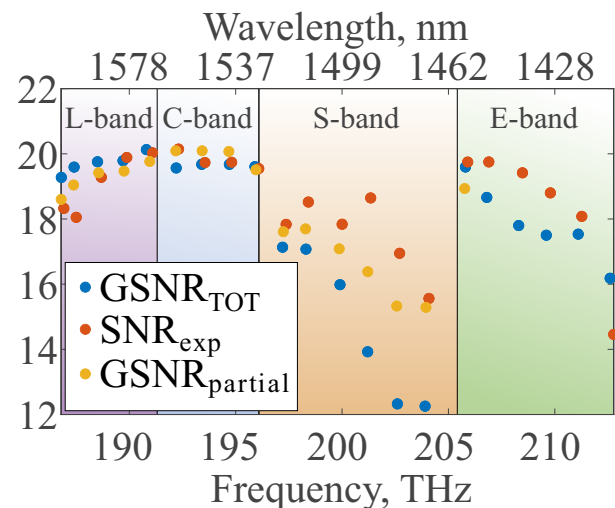

Fig. 12. The experimentally achieved SNR and numerically calculated GSNR values after propagation and amplification using the combined ESCL-band amplifier.

comparing this value to the OSNR and SNR_{NL} contributors given in Fig. 11. For example, the maximum $GSNR_{TOT}$ value is approximately 20 dB, whereas the OSNR and SNR_{NL} values lie between $25-30$ dB within the L- and C-bands.

A second observation is that the simulated GSNRs in the L-, C-, and E-bands are similar to that of the measured SNR_{exp}, with a maximum divergence of approximately 2 dB, 0.5 dB, and 2 dB for the least accurate predictions in each band, respectively. Furthermore, most of these values are conservative, except for the first three CUTs within the L-band, and the last CUT within the E-band. These discrepancies may primarily be explained by the differences between the experiment and the simulation, particularly the differences in launch powers impacting the SRS and NLI, along with uncertainty in the Raman pump powers, where fractions of a dB cause significant changes in the power profile evolution. The difference between the simulated and experimental results in the E-band primarily arises due to the former propagating a full spectral load, which gives an OSNR contribution much greater than the latter.

The S-band, however, has values that are up to approximately 3 dB lower than the experimental result. Comparing the results of the OSNR and SNR_{NL} to $GNSR_{TOT}$, it is evident that a significant amount of NLI has been generated in the S-band during the amplification process, which is due to the S-band channels entering the second IDF with large input powers. As only three channels in E-band were experimentally transmitted at any given time within the S-band experiment, the effects of SRS power transfer from the E- to the S-band in this case have been minimal. Lower SRS power transfer from the E- to S-band consequently causes less NLI to be produced in the S-band, therefore resulting in a better S-band performance. To confirm this latter assertion, we also modeled the experimental case, where only 4 channels (of which only one is a data-carrier) are present in the E-band. These results are presented in Figure 12, where it is seen that $GSNR_{partial}$ (4 E-band channels) is significantly higher in the S-band compared to the fully-loaded scenario $GSNR_{TOT}$.

From the results presented in this section, the implemented wideband model was shown to reliably recover the overall system performance by evaluating the total impairment, taking into consideration the linear, nonlinear, and transceiver impairments present within the experimental setup. The major difference between the experimental results and the simulation campaign performed in support of this work was that the E-band was simulated with a full spectral load, as opposed to a maximum of 4 channels available experimentally. This difference demonstrates that adding the E-band under full spectral load has a small performance impact upon the C- and L-bands, with the greatest impact arising from power transfer to the adjacent S-band. As a result, transmission over the entire LCSE bandwidth is a promising solution for rising capacity and throughput demands, and a promising next step to expand data transmission beyond L- and C-bands.

VII. Conclusion

Within this work we have experimentally demonstrated coherent transmission over a 25.83 THz (195 nm) bandwidth spanning the L-, C-, S- and partial E-bands with 150 30 GBaud DP-16-QAM channels, providing a potential for a total of 36 Tbit/s. Amplification has been performed with a hybrid amplifier that makes use of a DRA for the SCL-bands, and a BDFA for the E-band. A wideband model is then outlined and used to provide a QoT estimation for a full spectral load scenario and partial load (same as in the experiment) spectral load, finding that the main limiting propagation impairment is the NLI contribution within the S-band, arising primarily from the discrete Raman amplification process and SRS power transfer from the E-band.

These results show that the E-band presents a promising spectral region for wideband transmission due to the possibility of implementing low-noise amplification sources, although we observe that a robust power optimization technique is required to balance the impact of SRS and frequency-dependent fiber parameters. Making use of a per-channel power optimization which takes these parameters into account, along with the variability of the amplifier gain and NF values presents promising options for future work to provide a ESCL-band implementation with maximum possible GSNR.

References

[1] P. J. Winzer, D. T. Neilson, and A. R. Chraplyvy, "Fiber-optic transmission and networking: the previous 20 and the next 20 years," *Optics Express*, vol. 26, no. 18, pp. 24190–24239, 2018.

[2] I. Cristiani, C. Lacava, G. Rademacher, B. J. Puttnam, R. S. Luìs, C. Antonelli, A. Mecozzi, M. Shtaif, D. Cozzolino, D. Bacco *et al.*, "Roadmap on multimode photonics," *Journal of Optics*, vol. 24, no. 8, pp. 1–37, 2022.

[3] S. L. Olsson, J. Cho, S. Chandrasekhar, X. Chen, P. J. Winzer, and S. Makovejs, "Probabilistically shaped PDM 4096-QAM transmission over up to 200 km of fiber using standard intradyne detection," *Optics Express*, vol. 26, no. 4, pp. 4522–4530, 2018.

[4] X. Chen, J. Cho, A. Adamiecki, and P. Winzer, "16384-QAM transmission at 10 GBd over 25-km SSMF using polarization-multiplexed probabilistic constellation shaping," in *45th European Conference on Optical Communication (ECOC 2019)*. IET, 2019, pp. 1–4.

[5] A. D. Ellis, J. Zhao, and D. Cotter, "Approaching the non-linear Shannon limit," *Journal of lightwave technology*, vol. 28, no. 4, pp. 423–433, 2009.

[6] A. Ferrari, A. Napoli, J. K. Fischer, N. Costa, A. D'Amico, J. Pedro, W. Forysiak, E. Pincemin, A. Lord, A. Stavdas *et al.*, "Assessment on the achievable throughput of multi-band ITU-T G.652.D fiber transmission systems," *Journal of Lightwave Technology*, vol. 38, no. 16, pp. 4279–4291, 2020.

[7] L. Rapp and M. Eiselt, "Optical amplifiers for multi–band optical transmission systems," *Journal of Lightwave Technology*, vol. 40, no. 6, pp. 1579–1589, 2022.

[8] T. Hoshida, V. Curri, L. Galdino, D. T. Neilson, W. Forysiak, J. K. Fischer, T. Kato, and P. Poggiolini, "Ultrawideband systems and networks: Beyond C+L-band," *Proceedings of the IEEE*, vol. 110, no. 11, pp. 1725–1741, 2022.

[9] J. Renaudier, A. Napoli, M. Ionescu, C. Calo, G. Fiol, V. Mikhailov, W. Forysiak, N. Fontaine, F. Poletti, and P. Poggiolini, "Devices and fibers for ultrawideband optical communications," *Proceedings of the IEEE*, vol. 110, no. 11, pp. 1742–1759, 2022.

This article has been accepted for publication in IEEE/OSA Journal of Lightwave Technology. This is the author's version which has not been fully edited and content may change prior to final publication. Citation information: DOI 10.1109/JLT.2023.3339391

JOURNAL OF LIGHTWAVE TECHNOLOGY, VOL. 14, NO. 8, AUGUST 2021
12

[10] M. Jacques, Z. Xing, A. Samani, E. El-Fiky, X. Li, M. Xiang, S. Lessard, and D. V. Plant, "240 Gbit/s silicon photonic Mach-Zehnder modulator enabled by two 2.3-Vpp drivers," *Journal of Lightwave Technology*, vol. 38, no. 11, pp. 2877–2885, 2020.

[11] P. M. Seiler, G. Georgieva, G. Winzer, A. Peczek, K. Voigt, S. Lischke, A. Fatemi, and L. Zimmermann, "Toward coherent O-band data center interconnects," *Frontiers of Optoelectronics*, vol. 14, pp. 414–425, 2021.

[12] Y. Ososkov, A. Khegai, S. Firstov, K. Riumkin, S. Alyshev, A. Kharakhordin, A. Lobanov, A. Guryanov, and M. Melkumov, "Pump-efficient flattop O+E-bands bismuth-doped fiber amplifier with 116 nm–3 dB gain bandwidth," *Optics Express*, vol. 29, no. 26, pp. 44 138–44 145, 2021.

[13] J. W. Dawson, L. S. Kiani, P. H. Pax, G. S. Allen, D. R. Drachenberg, V. V. Khitrov, D. Chen, N. Schenkel, M. J. Cook, R. P. Crist *et al.*, "E-band Nd^{3+} amplifier based on wavelength selection in an all-solid micro-structured fiber," *Optics Express*, vol. 25, no. 6, pp. 6524–6538, 2017.

[14] U. C. de Moura, A. M. R. Brusin, A. Carena, D. Zibar, and F. Da Ros, "Simultaneous gain profile design and noise figure prediction for Raman amplifiers using machine learning," *Optics Letters*, vol. 46, no. 5, pp. 1157–1160, 2021.

[15] C. B. Gaur, V. Gordienko, F. Bessin, and N. J. Doran, "Dual-band amplification of downstream L-band and upstream C-band signals by FOPA in extended reach PON," in *2020 European Conference on Optical Communications (ECOC)*. IEEE, 2020, pp. 1–4.

[16] J. Renaudier, A. Arnould, A. Ghazisaeidi, D. Le Gac, P. Brindel, E. Awwad, M. Makhsiyan, K. Mekhazni, F. Blache, A. Boutin *et al.*, "Recent advances in 100+ nm ultra-wideband fiber-optic transmission systems using semiconductor optical amplifiers," *Journal of Lightwave Technology*, vol. 38, no. 5, pp. 1071–1079, 2020.

[17] P. Hazarika, M. Tan, A. Donodin, S. Noor, I. Phillips, P. Harper, J. S. Stone, M. J. Li, and W. Forysiak, "E-, S-, C-and L-band coherent transmission with a multistage discrete Raman amplifier," *Optics Express*, vol. 30, no. 24, pp. 43 118–43 126, 2022.

[18] A. Donodin, E. Manuylovich, V. Dvoyrin, M. Melkumov, V. Mashinsky, and S. Turitsyn, "38 dB gain E-band bismuth-doped fiber amplifier," in *48th European Conference on Optical Communication (ECOC 2022)*. IEEE, 2022, pp. 1–3.

[19] N. Thipparapu, Y. Wang, A. Umnikov, P. Barua, D. Richardson, and J. Sahu, "40 dB gain all fiber bismuth-doped amplifier operating in the O-band," *Optics Letters*, vol. 44, no. 9, pp. 2248–2251, 2019.

[20] A. Donodin, V. Dvoyrin, E. Manuylovich, L. Krzczanowicz, W. Forysiak, M. Melkumov, V. Mashinsky, and S. Turitsyn, "Bismuth doped fibre amplifier operating in E- and S-optical bands," *Optical Materials Express*, vol. 11, no. 1, pp. 127–135, 2021.

[21] S. Firstov, V. Khopin, I. Bufetov, E. Firstova, A. Guryanov, and E. Dianov, "Combined excitation-emission spectroscopy of bismuth active centers in optical fibers," *Optics Express*, vol. 19, no. 20, pp. 19 551–19 561, 2011.

[22] Y. Wang, S. Wang, A. Halder, and J. Sahu, "Bi-doped optical fibers and fiber amplifiers," *Optical Materials: X*, vol. 17, pp. 1–12, 2023.

[23] A. Donodin, M. Tan, P. Hazarika, V. Dvoyrin, I. Phillips, P. Harper, S. K. Turitsyn, and W. Forysiak, "30-GBaud DP 16-QAM transmission in the E-band enabled by bismuth-doped fiber amplifiers," *Optics Letters*, vol. 47, no. 19, pp. 5152–5155, 2022.

[24] A. Donodin, P. Hazarika, M. Tan, V. Dvoyrin, M. Patel, I. Phillips, P. Harper, S. Turitsyn, and W. Forysiak, "195-nm multi-band amplifier enabled by bismuth-doped fiber and discrete Raman amplification," in *2022 European Conference on Optical Communications (ECOC)*. IEEE, 2022, pp. 1–4.

[25] A. D'Amico, B. Correia, E. London, E. Virgillito, G. Borraccini, A. Napoli, and V. Curri, "Scalable and disaggregated GGN approximation applied to a C+L+S optical network," *Journal of Lightwave Technology*, vol. 40, no. 11, pp. 3499–3511, 2022.

[26] J. K. Fischer, M. Cantono, V. Curri, R.-P. Braun, N. Costa, J. Pedro, E. Pincemin, P. Doaré, C. Le Bouëtté, and A. Napoli, "Maximizing the capacity of installed optical fiber infrastructure via wideband transmission," in *2018 20th International Conference on Transparent Optical Networks (ICTON)*. IEEE, 2018, pp. 1–4.

[27] P. Poggiolini, "The GN model of non-linear propagation in uncompensated coherent optical systems," *Journal of Lightwave Technology*, vol. 30, no. 24, pp. 3857–3879, 2012.

[28] A. Ferrari, M. Filer, K. Balasubramanian, Y. Yin, E. Le Rouzic, J. Kundrát, G. Grammel, G. Galimberti, and V. Curri, "GNPy: an open source application for physical layer aware open optical networks," *Journal of Optical Communications and Networking*, vol. 12, no. 6, pp. C31–C40, 2020.

[29] "GitHub repository of GNPy." [Online]. Available: https://github.com/Telecominfraproject/oopt-gnpy

[30] P. Hazarika, M. Tan, A. Donodin, I. Phillips, P. Harper, M.-J. Li, and W. Forysiak, "210 nm E, S, C and L band multistage discrete Raman amplifier," in *Optical Fiber Communication Conference*. Optica Publishing Group, 2022, pp. 1–3.

[31] A. E. El-Taher, J. D. Ania-Castañón, V. Karalekas, and P. Harper, "High efficiency supercontinuum generation using ultra-long Raman fiber cavities," *Optics Express*, vol. 17, no. 20, pp. 17 909–17 915, 2009.

[32] R. Emmerich, M. Sena, R. Elschner, C. Schmidt-Langhorst, I. Sackey, C. Schubert, and R. Freund, "Enabling SCL-band systems with standard C-band modulator and coherent receiver using coherent system identification and nonlinear predistortion," *Journal of Lightwave Technology*, vol. 40, no. 5, pp. 1360–1368, 2021.

[33] P. Skvortcov, I. Phillips, W. Forysiak, T. Koike-Akino, K. Kojima, K. Parsons, and D. S. Millar, "Nonlinearity tolerant LUT-based probabilistic shaping for extended-reach single-span links," *IEEE Photonics Technology Letters*, vol. 32, no. 16, pp. 967–970, 2020.

[34] A. Ellis, M. McCarthy, M. Al Khateeb, M. Sorokina, and N. Doran, "Performance limits in optical communications due to fiber nonlinearity," *Advances in Optics and Photonics*, vol. 9, no. 3, pp. 429–503, 2017.

[35] N. Taengnoi, K. R. Bottrill, Y. Hong, Y. Wang, N. K. Thipparapu, J. K. Sahu, P. Petropoulos, and D. J. Richardson, "Experimental characterization of an O-band bismuth-doped fiber amplifier," *Optics Express*, vol. 29, no. 10, pp. 15 345–15 355, 2021.

[36] M. A. Iqbal, P. Harper, and W. Forysiak, "Improved design of ultra-wideband discrete Raman amplifier with low noise and high gain," in *Nonlinear Photonics*. Optical Society of America, 2018, pp. 1–3.

[37] L. Krzczanowicz, M. A. Z. Al-Khateeb, M. A. Iqbal, I. Phillips, P. Harper, and W. Forysiak, "Performance estimation of discrete Raman amplification within broadband optical networks," in *Optical Fiber Communication Conference*. Optica Publishing Group, 2019, pp. 1–3.

[38] M. A. Iqbal, M. A. Z. Al-Khateeb, L. Krzczanowicz, I. D. Phillips, P. Harper, and W. Forysiak, "Linear and nonlinear noise characterisation of dual stage broadband discrete Raman amplifiers," *J. Lightw. Technol.*, vol. 37, no. 14, pp. 3679–3688, 2019.

[39] D. Gloge, "Weakly guiding fibers," *Applied Optics*, vol. 10, no. 10, pp. 2252–2258, 1971.

[40] I. H. Malitson, "Interspecimen comparison of the refractive index of fused silica," *JOSA*, vol. 55, no. 10, pp. 1205–1209, 1965.

[41] J. Bromage, "Raman amplification for fiber communications systems," *Journal of Lightwave Technology*, vol. 22, no. 1, pp. 79–93, 2004.

[42] D. Semrau, E. Sillekens, P. Bayvel, and R. I. Killey, "Modeling and mitigation of fiber nonlinearity in wideband optical signal transmission," *Journal of Optical Communications and Networking*, vol. 12, no. 6, pp. C68–C76, 2020.

[43] D. Semrau, R. I. Killey, and P. Bayvel, "A closed-form approximation of the Gaussian noise model in the presence of inter-channel stimulated Raman scattering," *Journal of Lightwave Technology*, vol. 37, no. 9, pp. 1924–1936, 2019.

[44] C. Lasagni, P. Serena, and A. Bononi, "A Raman-aware enhanced GN-model to estimate the modulation format dependence of the SNR tilt in C+L band," in *45th European Conference on Optical Communication (ECOC 2019)*. IET, 2019, pp. 1–4.

[45] A. D'Amico, E. London, E. Virgillito, A. Napoli, and V. Curri, "Quality of transmission estimation for planning of disaggregated optical networks," in *2020 International Conference on Optical Network Design and Modeling (ONDM)*. IEEE, 2020, pp. 1–3.

[46] D. Pilori, M. Cantono, A. Carena, and V. Curri, "FFSS: The fast fiber simulator software," in *2017 19th International Conference on Transparent Optical Networks (ICTON)*. IEEE, 2017, pp. 1–4.

[47] D. Marcuse, C. Manyuk, and P. K. A. Wai, "Application of the Manakov-PMD equation to studies of signal propagation in optical fibers with randomly varying birefringence," *Journal of Lightwave Technology*, vol. 15, no. 9, pp. 1735–1746, 1997.

[48] E. London, E. Virgillito, A. D'Amico, A. Napoli, and V. Curri, "Simulative assessment of non-linear interference generation within disaggregated optical line systems," *OSA continuum*, vol. 3, no. 12, pp. 3378–3389, 2020.

[49] C. R. Menyuk and B. S. Marks, "Interaction of polarization mode dispersion and nonlinearity in optical fiber transmission systems," *Journal of Lightwave Technology*, vol. 24, no. 7, pp. 2806–2826, 2006.

[50] F. Hamaoka, M. Nakamura, S. Okamoto, K. Minoguchi, T. Sasai, A. Matsushita, E. Yamazaki, and Y. Kisaka, "Ultra-Wideband WDM Transmission in S-, C-, and L-Bands Using Signal Power Optimization

Scheme," *Journal of Lightwave Technology*, vol. 37, no. 8, pp. 1764–1771, 2019.

[51] B. Correia, R. Sadeghi, E. Virgillito, A. Napoli, N. Costa, J. Pedro, and V. Curri, "Power control strategies and network performance assessment for C+L+S multiband optical transport," *Journal of Optical Communications and Networking*, vol. 13, no. 7, pp. 147–157, 2021.

[52] P. Poggiolini, G. Bosco, A. Carena, R. Cigliutti, V. Curri, F. Forghieri, R. Pastorelli, and S. Piciaccia, "The LOGON strategy for low-complexity control plane implementation in new-generation flexible networks," in *Optical Fiber Communication Conference*. Optica Publishing Group, 2013, pp. 1–3.

[53] F. Pezoa, J. L. Reutter, F. Suarez, M. Ugarte, and D. Vrgoč, "Foundations of JSON schema," in *Proceedings of the 25th international conference on World Wide Web*, 2016, pp. 263–273.

[54] A. D'Amico, E. London, E. Virgillito, A. Napoli, and V. Curri, "Inter-band GSNR degradations and leading impairments in C+ L band 400G transmission," in *2021 International Conference on Optical Network Design and Modeling (ONDM)*. IEEE, 2021, pp. 1–3.

[55] V. Ingle, S. Kogon, and D. Manolakis, *Statisical and adaptive signal processing*. Artech, 2005.